European Journal of Cell Biology 104 (2025) 151502

Contents lists available at ScienceDirect

European Journal of Cell Biology

journal homepage: www.elsevier.com/locate/ejcb

Integrated phenotypic and transcriptomic characterization of desmin-related cardiomyopathy in hiPSC-derived cardiomyocytes and machine learning-based classification of disease features☆

Vivien Batoumeni [a,b], Yeranuhi Hovhannisyan [b], Bénédicte Gobert [a], Keyhan Alvandipour [a], Jennifer Arthur Ataam [a], Ombline Conrad [a], David Hoffmann [a], Nicolas Wiest-Daesslé [a], Jochen Dobner [c], José Américo Nabuco Leva Ferreira Freitas [b], Hakim Hocini [d], Zhenlin Li [b], Laurent Brino [a], Andrea Rossi [c], Onnik Agbulut [b,*], Peter Sommer [a], Pierre Joanne [b,♯], Konstantinos Gkatzis [a,*,♯]

[a] Ksilink, Strasbourg F-67000, France
[b] Sorbonne Université, Institut de Biologie Paris-Seine (IBPS), UMR CNRS 8263, INSERM U1345, Development, Adaptation and Ageing, Paris F-75005, France
[c] Leibniz Research Institute for Environmental Medicine, Auf'm Hennekamp 50, Düsseldorf D-40225, Germany
[d] Université Paris-Est Créteil, INSERM U955, Créteil F-94010, France

ARTICLE INFO

keywords:
Machine Learning
Disease Modeling
Myofibrillar Myopathy
Desminopathy
Dilated Cardiomyopathy
Cardiomyocyte

ABSTRACT

Desmin-related diseases are characterized by skeletal muscle weakness, cardiomyopathy, and respiratory dysfunction due to mutations in the desmin gene (*DES*), which encodes a protein essential for muscle cell integrity. This study investigates the effects of a pathogenic desmin mutation (DES^{E439K}) in human cardiomyocytes derived from human induced pluripotent stem cells (hiPSCs) obtained from a patient carrying the DES^{E439K} mutation, compared to cardiomyocytes derived from hiPSCs of three healthy donors. To further validate our findings a genome edited cell line has been obtained following the insertion of the mutation in a control hiPSC line. Using advanced technologies, including transcriptomics and phenotypic machine learning algorithms, we analyzed how this mutation disrupts cellular function and contributes to disease phenotypes. Our findings reveal that cardiomyocytes carrying DES^{E439K} exhibit cytoplasmic protein aggregation, mitochondrial and sarcomere defects, and contractile dysfunctions, highlighting key phenotypic defects in desmin-related cardiomyopathy. Finaly, we developed a machine learning prediction model to classify cellular phenotypes, which can be used for translational research, including drug candidate screening. This research opens new avenues for understanding the molecular mechanisms of desmin-related cardiomyopathies and fosters the development of novel therapeutic strategies.

1. Introduction

Desmin-related genetic disorders are characterized by skeletal muscle weakness, cardiomyopathy, and respiratory dysfunction. The underlying cause of these diseases are mutations in the *DES* gene, which encodes desmin, a type III intermediate filament protein, crucial for maintaining the structural integrity and proper function of muscle cells (Brodehl et al., 2018). Mutations often lead to the formation of desmin-positive aggregates in the cytoplasm, which disrupt the normal architecture and function of cardiomyocytes and skeletal muscle cells by

Abbreviations: ACTN2, sarcomeric α-actinin; DCM, dilated cardiomyopathy; EHTs, Engineered heart tissues; HiPSCs, Human induced pluripotent stem cells; HiPSC-CMs, Cardiomyocytes derived from human induced pluripotent stem cells; LDA, Linear Discriminant Analysis; MM1, Maturation media 1; MM2, Maturation media 2; MYL2, Myosin light chain 2; PCA, Principal component analysis; ROI, Region of interest; RT, resting tension; TMRM, tetramethylrhodamine methyl ester; TNNT2, cardiac troponin T.

☆ All authors contributed to the final manuscript.

* Corresponding authors.
E-mail addresses: onnik.agbulut@sorbonne-universite.fr (O. Agbulut), konstantinosgkatzis@gmail.com (K. Gkatzis).
♯ These authors contributed equally.

https://doi.org/10.1016/j.ejcb.2025.151502
Received 11 March 2025; Received in revised form 8 June 2025; Accepted 28 June 2025
Available online 1 July 2025

interfering with critical cellular processes such as mitochondrial function, calcium signaling and muscle contraction (Capetanaki et al., 2015). At the cardiac level, patients carrying a *DES* mutation often experience arrhythmias, heart failure, with some patients succumbing to sudden cardiac death (Ebrahim et al., 2025).

Desmin and its multiple binding partners form a 3D scaffold that spans the entire diameter of the cardiomyocyte, surrounding the Z-discs linking the contractile apparatus to the costameres and intercalated discs of the plasma membrane, as well as to most membrane-bound cellular organelles, including mitochondria, the sarcoplasmic reticulum and the nucleus (Fig. 1**A**). Thus, desmin is necessary to maintain mechanical stability of muscle cells, facilitating force transmission during muscle contraction (Capetanaki et al., 2015; Tsikitis et al., 2018). The pathogenicity of desmin mutations encompasses a spectrum of molecular dysfunctions, including alteration of extra-sarcomeric intermediate filament network due to co-aggregation of mutant and wild-type desmin, resulting in compromised mitochondrial functions, cell signaling cascades, protein quality control, and cellular mechanics (Hnia et al., 2015). Other mutations result in the production of functionally impaired desmin that cannot properly integrate into the filament network, or exert a dominant-negative effect through the formation of toxic aggregates (Brodehl et al., 2019; Carlsson et al., 2002; Chourbagi et al., 2011; Goldfarb et al., 1998; Joanne et al., 2013; Wang et al., 2001).

Current treatments for desmin-related cardiomyopathies primarily focus on symptom management and slowing disease progression, with few options targeting the underlying genetic and molecular causes (Schultheiss et al., 2019). Given the complexity of these cardiomyopathies, there is a critical need for innovative therapeutic approaches that directly address the molecular mechanisms of disease.

Recent advancements in biotechnology, including the use of induced pluripotent stem cells (iPSCs), genome editing, and three-dimensional tissue engineering, have opened new avenues for the detailed study and potential treatment of muscular diseases (Brodehl et al., 2019; Camman et al., 2022). In this study, we leverage advanced technologies to investigate the effects of *DES* mutations in human iPSC-derived cardiomyocytes (hiPSC-CMs), focusing on a pathogenic G-to-A transition at c.1315 (codon 439) in exon 8 of the *DES* gene, resulting in a glutamic acid to lysine substitution at position 439 at the C-terminus of desmin. Using transcriptomics and phenotypic machine learning algorithms, we analyze how this mutation disrupts cellular function, contributes to disease phenotypes, and predicts cellular responses to potential therapeutic interventions. Our findings indicate that mutant *DES* hiPSC-CMs exhibit pathogenic proteinopathy, mitochondrial and sarcomere defects, and contractile dysfunctions, revealing multiple phenotypic defects that characterizes desmin-related cardiomyopathies pathogenesis. Using defects in multiple cellular functions, we successfully developed a machine learning prediction model that can be used for translational research including screening of libraries of potential drug candidates, prediction of the efficacy of drug candidates, the design of new drug candidates and the assessment of the toxicity of drug candidates.

Therefore, the results and technologies described here open new avenues for translational efforts towards a better understanding of the molecular disease pathology causally linked to cardiac disease manifestations of *DES* mutations and have the potential to foster the discovery and development of new therapeutic options to address an unmet medical need.

In this study, to comprehensively assess the impact of the DES^{E439K} mutation on cardiomyocyte structure and function, we designed a multilayered experimental workflow. We first examined morphological changes using immunostainings and then performed functional analyses using engineered heart tissues (EHTs) to evaluate the physiological consequences of the mutation on contractility. This was followed by transcriptomic profiling to provide insight into the molecular pathways underlying the observed phenotypes, and finally, we conducted a detailed evaluation of cellular morphology using high-content imaging and applied machine learning algorithms to identify and classify phenotypic alterations at the single-cell level. This stepwise approach enabled us to link cellular morphology, function, and gene expression, thereby offering a robust and integrated understanding of desmin-related cardiomyopathy. Collectively, the results and technologies described here open new avenues for translational efforts towards a better understanding of the molecular disease pathology causally linked to cardiac disease manifestations of desmin mutations and have the potential to foster the discovery and development of new therapeutic options to address an unmet medical need.

2. Material and methods

2.1. hiPSC and cardiomyocyte differentiation

Six different cell lines were used in this study. Among them we have used 3 different wild-type (WT) cell lines derived from 3 healthy donors: WT hiPSC 1 (Healthy control 1), WT hiPSC 2 (Healthy control 2) and WT hiPSC 3 (DES^{WT}). We also used three different mutant cell lines carrying the heterozygous DES^{E439K} variant generated previously (Hovhannisyan et al., 2024). Among them, two were derived from one patient carrying this mutation ($pDES^{HET}$ clone 1 and $pDES^{HET}$ clone 2) and the last was created by genome editing in hiPSC derived from the DES^{WT} cell line (DES^{HET}) as previously described in (Hovhannisyan et al., 2024).

All cell lines were maintained in StemMACS Brew (Miltenyi Biotech) or E8 (Thermofisher Scientific) and passaged twice a week using TrypLE select. hiPSCs were differentiated into beating cardiomyocytes (hiPSC-CMs) with a modified small molecule-based monolayer method (Lian et al., 2012). Following differentiation, human hiPSC-CMs were cultured in a medium described in (Laco et al., 2020) composed of RPMI-1640 with Glutamax, 1 % 100 × penicillin/streptomycin (Thermo Fisher Scientific), 1 % 100 × sodium pyruvate (Thermo Fisher Scientific), 200 μM L-ascorbic acid 2 phosphate sesquimagnesium salt hydrate (Sigma-Aldrich, USA), 2 % B27 supplement (Thermo Fisher Scientific). In addition, we also have tested two different maturation media (MM1 and MM2). MM1 is similar to the normal medium in which was added thyroid hormone triiodothyronine (Thermofisher Scientific) at 100 nM and dexamethasone (Tocris) at 1 μM. Finally, MM2 is composed of DMEM no Glucose (Gibco); 1X B27 Supplement (Gibco); 1X Non-Essential Amino Acids (Gibco); 250 U/ml penicillin-streptomycin (Gibco); 0.5 % KnockOut Serum Replacement (Gibco); 3 mM Glucose (Sigma); 10 mM L-lactate sodium (Sigma); 5 mM Creatine monohydrate (Sigma); 0,5 % Albumax I (Gibco); Vitamin B12 (Sigma); 0.82 μM Biotin (Sigma), 2 mM Taurine (Sigma), 2 mM L-Carnitine (Sigma); 0.5 M Ascorbic Acid (Sigma) (Feyen et al., 2020).

hiPSC-CMs expressed typical cardiac markers such as cardiac troponin T (TNNT2), sarcomeric α-actinin (ACTN2), and myosin light chain 2 (MYL2). Following 25 days of cardiac differentiation, beating hiPSC-CM monolayers were dissociated using TrypLE Select (Thermofisher Scientific) and plated in the required assay format. Informed consent was obtained from all participants as previously described (Hovhannisyan et al., 2024) and all research was performed in accordance with relevant guidelines and regulations.

2.2. Image analysis and machine learning

Cells were fixed with 4 % formaldehyde for 20 min at room temperature, followed by permeabilization and blocking with (10 % BSA, 0.5 % Triton X-100 in PBS) and incubation with primary antibodies (Supplementary Table S1**)** diluted in (1 % BSA in PBS) overnight at 4°C. Cells were washed with PBS and incubated with secondary antibodies for 2 h at room temperature. For live cell imaging, tetramethylrhodamine methyl ester (TMRM) or Mitotracker dyes were added into prewarmed complete media and incubated for 45 min at 37°C 5 % CO_2, followed by 3 washes with cell culture medium. Images were taken with a CV7000 (Yokogawa) microscope in scanning confocal mode using a

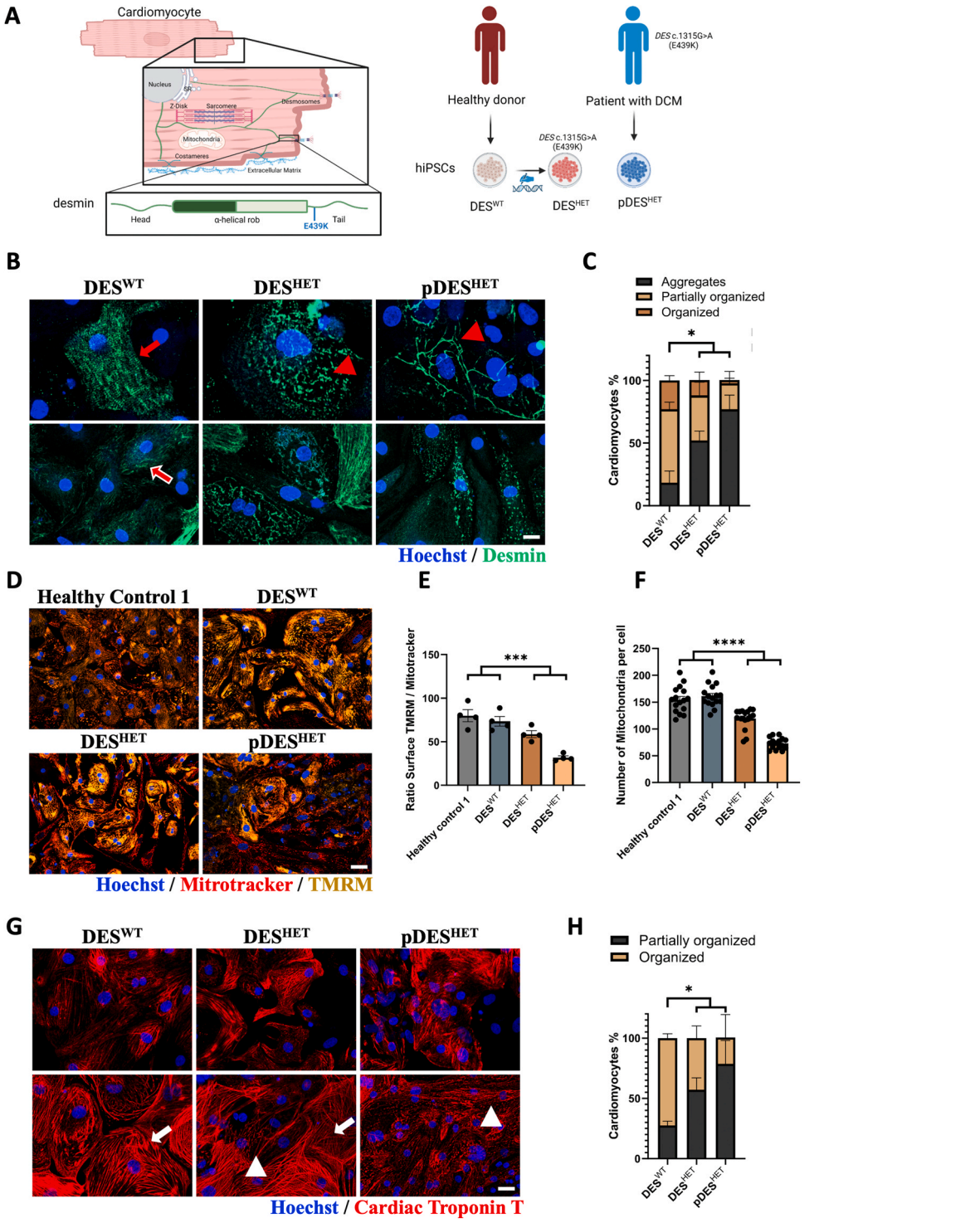

(caption on next page)

Fig. 1. Morphological characterization of hiPSC-CMs carrying *DES*^{E439K} mutation. A. (Left) Schematic overview of the localization of desmin filaments (green) in cardiomyocytes. Desmin filaments connect several protein-protein complexes (*e.g.*, desmosomes, Z-band) and cell organelles (mitochondria, nuclei) to the cytoskeletal network. (Right) Human induced pluripotent stem cells (hiPSCs) from healthy donors (DES^{WT} or Healthy control 1) and carrying the heterozygous *DES*^{E439K} variant that were either isolated from a patient (pDES^{HET}) or generated by gene editing (DES^{HET}) were differentiated into cardiomyocytes. **B.** Immunofluorescence images of nuclei (Hoechst, Blue) and cardiac desmin in WT (DES^{WT}) and two DES (DES^{HET} and pDES^{HET} clone 1) cardiomyocytes, illustrating 3 different levels of desmin organization (organized indicated by red arrow, partially organized indicated by red arrow with white outline and aggregates indicated with red arrowhead. Scale bars, 10 μm. **C.** Percentage of hiPSC-CMs with organized, partially organized and aggregates of desmin organization from one WT (DES^{WT}) and two DES (DES^{HET} and pDES^{HET} clone 1) lines. Statistical difference was tested using two-tailed Student's *t*-test of aggregated values (Control 2, n = 30; DES^{HET}, n = 53; pDES^{HET} clone 1, n = 35, $*p < 0.05$). **D.** Immunofluorescence images of Mitotracker and TMRM in WT (Healthy control 1 and DES^{WT}) and DES (DES^{HET} and pDES^{HET} clone 1) cardiomyocytes. Higher magnification of these images is provided in Supplementary Fig. S4. Scale bars, 10 μm. **E.** Ratio surface TMRM signal normalized by Mitotracker signal in WT (Healthy control 1 and DES^{WT}) and DES (DES^{HET} and pDES^{HET} clone 1) cardiomyocytes. Statistical difference was tested using two-tailed *t*-test of WT and *DES*^{E439K} ($***p < 0.0005$). **F.** Mitochondria count per cell from WT (Healthy control 1 and DES^{WT}) and *DES*^{E439K} (DES^{HET} and p*DES*^{HET} clone 1) cardiomyocytes. Statistical difference was tested using two-tailed *t*-test of WT and *DES*^{E439K} ($****p < 0.0001$). **G.** Immunofluorescence images of cardiac Troponin T in WT (DES^{WT}) and *DES*^{E439K} (DES^{HET} and pDES^{HET} clone 1) cardiomyocytes, illustrating 2 different levels of sarcomeric organization (organized, white arrow and partially organized, white arrowhead). Higher magnification of these images is provided in supplementary Fig. S5. Scale bars, 10 μm. **H.** Percentage of cells with different levels of sarcomeric organization. Statistical difference was tested using two-tailed Student's *t*-test of partially organized cardiac Troponin T values (Control 2, n = 498; DES^{HET}, n = 348; pDES^{HET}, n = 443, $*p < 0.05$).

dual Nipkow disk. 384-well plates (Phenoplate, Perkin Elmer) were mounted on a motorized stage and images were acquired in a row-wise ''zigzag'' fashion at RT for fixed cells. The system's software (CellVoyager) and solid laser lines (405/488/561/640 nm) was used to acquire 3 Z-plane (1μm shifting) 16-bit TIFF images through a dry 40x objective lens using a cooled sCMOS camera with 2560 × 2160 pixels and a pixel size of 6.5 mm without pixel binning. The 3 Z-plane are fused with maximum projection. Nine images in a 3 × 3 matrix pattern were acquired from the center of each well.

Image analysis pipelines were developed using the open-source PhenoLINK software (Phenolink https://github.com/Ksilink/PhenoLink) developed by KSILINK. Briefly, images were segmented to identify individual cells, with nuclei positions determined using a reference channel (Hoechst staining). Each nucleus (crop) was assigned a unique label, and further segmentation with additional channels generated accurate masks for cells and cytoplasm. Morphological properties (size, shape, texture, features, intensity, local density, radial distributions) of each identified crop were calculated. Most data analysis and graphical presentations were performed using Python via the Jupyter Notebook interface. The open-source machine learning library scikit-learn (open-source ML library) was mainly used for data processing and feature selection based on statistical significance. The supplementary table S2 include the full list of features and their biological relevance. The pandas and numpy libraries were utilized for mathematical data processing, while the plotly.express library was employed for data visualization and graphing. Each data point represents the mean of a single well in a 384-well plate, comprising nine images per well.

2.3. Generation of engineered heart muscle tissue

Engineered heart tissues (EHTs) were generated using a modified version of a previously published protocol (Tiburcy et al., 2017). Briefly, EHTs (reconstitution volume: 185 μl) were prepared by combining freshly dispersed hiPSC-CMs (purity > 90 %) with fibroblasts (HFF-1, ATCC, SCRC-1041) at a 70:30 ratio. The mixture also included pH-neutralized rat tail collagen type I (0.4 mg/EHT), Matrigel™ (10 % v/v; Becton Dickinson), and concentrated serum-containing culture medium (2 × DMEM, 20 % horse serum, 4 % chicken embryo extract, 200 U/ml penicillin, and 200 μg/ml streptomycin). The mixture was distributed into each well of a 48-well EHT multi-well plate (myrPlate-TM5; Myriamed GmbH) and incubated at 37°C for approximately 45 min. Afterwards, EHT medium freshly supplemented with TGFβ1 (Peprotech, AF-100–21C) was added. During the initial three days, the tissue medium was refreshed daily with EHT medium containing TGFβ1. For the remainder of the experiment, the medium was replaced daily with EHT medium alone. Contraction measurements were performed using video-optical recordings of EHT-mediated pole bending in a myrPlate-TM5 culture format at 37 °C. Spontaneous contractions were recorded for at least 2 min at 50 fps at specified time points using a myrImager prototype (Myriamed GmbH). Percent pole bending served as a surrogate measure for contraction force (F). Contraction and relaxation times were measured from 20 % to 80 % peak contraction and relaxation, respectively. Contraction and relaxation velocities were reported as maximal and minimal dF/dt.

2.4. RNA isolation and RT-qPCR analysis

RNA was isolated from hiPSC-CMs cultured in a 384-well plate format using the NucleoSpin RNA XS Micro Kit (MACHEREY-NAGEL) following the manufacturer's instructions. Real-time PCR was performed using the TaqMan gene expression assay (Applied Biosystems), incorporating TaqMan Fast Advanced Master Mix 1 × (ThermoFisher) and gene-specific TaqMan assay probes (ThermoFisher) labeled with fluorophore tags. Quantitative PCR (qPCR) was conducted on a QuantStudio 5 Real-Time PCR Instrument (Applied Biosystems).

2.5. Double-stranded cDNA synthesis and amplification for RNAseq

RNA samples were subjected to first strand cDNA synthesis in 0.2 ml DNA Lo-Bind tubes (Eppendorf) in a 6 μl reaction containing 200 ng total RNA, 2 μl 10 μM RT primer (5'->3': AAG CAG TGG TAT CAA CGC AGA GTA CTT TTT TTT TTT TTT TTT TTT TTT TTT TV), 1 μl 10 mM each dNTPs (Vazyme) and aqua dest for five min at 70 °C. Aftewards, samples were snap frozen and subjected to reverse transcription and template switching by adding 2.5 μl 4x template switching buffer (New England Biolabs), 0.5 μl 75 μM Template Switching Oligo (5'->3': GCT AAT CAT TGC AAG CAG TGG TAT CAA CGC AGA GTA CAT rGrGrG) and 1 μl Template Switching Enzyme mix (New England Biolabs) and incubation for 90 min at 42 °C, followed by five min at 85 °C. Subsequently, double stranded cDNA (dscDNA) was amplified by adding 25 μl 2 x Phanta Max Buffer (Vazyme), 1 μl 10 mM each dNTPs (Vazyme), 2 μl 100 U/μl Phanta Max Super Fidelity Polymerase (Vazyme), 1 μl 10 μM cDNA PCR amplification primer (5'->3': AAG CAG TGG TAT CAA CGC AGA GT) and 11 μl aqua dest. and performing a PCR reaction (45 sec at 98 °C, followed by 8 cycles of 10 sec at 98 °C, 15 sec at 62 °C and 3 min at 72 °C with a final elongation of 5 min at 72 °C and storage at 4 °C). 1 μl 20 U/μl Exonuclease I (ThermoFisher) was added directly to each reaction and incubated for 15 min at 37 °C and for 15 min at 80 °C. PCR products were pooled per sample and cleaned up using AMPure XP beads (Beckham Coulter) at a ratio of 0.8 X DNA: beads. Concentration was measured on a Qubit Fluorometer (ThermoFisher) with the dsDNA high sensitivity kit (ThermoFisher).

2.6. Library preparation and long-read RNAseq

Library preparation was carried out using the Native Barcoding Kit

24 V14 (Oxford Nanopore Technologies) according to the protocol version NBA_9168_v114_revE_15Sep2022. Equal amounts of dscDNA were used for library preparation and the final library was quantified on a Qubit Fluorometer using the dsDNA high sensitivity kit. Library size was checked on a D5000 High Sensitivity Screen Tape (Agilent) on a Tape Station 4200 (Agilent). A total of 15 fmol were loaded onto a P2 solo (Oxford Nanopore Technologies) using a PromethION flow cell (Oxford Nanopore Technologies). Library was sequenced for 72 h. Afterwards, basecalling was performed using Guppy (version 6.4.6) and the reads aligned using minimap2 (version 2.24) with the options -ax splice –secondary=no against the human reference genome (GRCh38).

2.7. RNA Sequencing data analysis

Sequencing data analysis was performed using R (version 4.2.2), Rsubread (version 2.12.3) feature counts with the option for long sequencing reads to count transcripts and annotated with GRCh38 build 106. Reads were normalized to counts per million and differential gene expression analysis performed using edgeR (version 3.40.2). Gene Set Enrichment Analysis was performed using clusterProfiler (version 4.6.2) gseGO with a p-value cutoff of 0.05. Data was visualized using ggplot2 (version 3.4.2) and ComplexHeatmap (version 2.14).

2.8. Data analysis and statistics

Data are expressed as mean ± standard error of the mean (SEM). Comparisons between two groups were analyzed using two-sided unpaired or paired Student's *t*-tests. For comparisons involving three or more groups, one-way or two-way ANOVA, with or without repeated measures, was applied, followed by the appropriate post-hoc tests. Details of the statistical tests used are provided in the respective figure legends. All statistical analyses were conducted using GraphPad Prism version 9.5.1.

3. Results

3.1. Characterization of hiPSC-derived cardiomyocytes carrying a heterozygous pathogenic desmin variant DES^{E439K}

To investigate the effects of a pathogenic heterozygous desmin mutation in human cardiomyocytes, we have used hiPSCs from a patient ($pDES^{HET}$ clone 1 and $pDES^{HET}$ clone 2) carrying a heterozygous single nucleotide (G to A) transition at c1315 (codon 439) leading to a substitution of glutamic acid by lysine in position 439 at the C-terminal end of desmin (DES^{E439K}). An isogenic pair (DES^{WT} and DES^{HET}) with the same heterozygous mutation was also used (Fig. 1**A**) (Hovhannisyan et al., 2024)**.** Cardiomyocyte differentiation was conducted using a monolayer-based protocol by modulating Wnt signaling pathways. Wild-type (WT) and DES^{E439K} (DES^{HET} and $pDES^{HET}$) hiPSC lines all produced high-purity hiPSC-CMs consisting predominantly of cardiac troponin T $(TNNT2)^{+}$ / myosin light chain 2 $(MYL2)^{+}$ ventricular-like cells (Figure S1). Under monolayer culture conditions, we noticed that desmin expression depends on the maturation state of the cardiomyocytes, thus we evaluated three culture conditions, including classical media (RPMI based) and two culture media that have been reported to increase the maturation of the cardiomyocytes (MM1 and MM2) (Feyen et al., 2020). We found increasing desmin expression as cardiomyocytes mature *in vitro* with MM1 at later time point (Figure S2). It should be noted that this medium comprised T3 and dexamethasone, indicating that these molecules may have a role in the induction of expression of desmin.

To better understand the cellular mechanisms underlying the dilated cardiomyopathy (DCM)-like phenotype in DES^{E439K} hiPSC-CMs, we examined the intracellular localization of the mutant protein. Under optimal MM1 culture conditions, DES^{E439K} hiPSC-CMs displayed differences in a number of cellular profiles by image-based analysis (Fig. 1**B-H**). We created a dataset that were manually segmented and assigned a desmin organization score by two experts. Each cell was scored as aggregates (desmin staining is sparse or display punctate structures), partially organized (part of cell area is covered by striated patterns of the desmin staining) and organized (desmin is striated with the majority of cell area covered) (Fig. 1**B**). Notably, we observed heterogeneity in the organization of the desmin filaments in both WT and DES^{E439K} hiPSC-CMs, with more desmin aggregates in DES^{HET} and $pDES^{HET}$ hiPSC-CMs (Fig. 1**C**).

We and others have previously demonstrated that structural and functional alterations of mitochondria are a hallmark of desmin-related cardiomyopathy (Hovhannisyan et al., 2024; Smolina et al., 2020). Thus, we focused on the development of a readout taking into account the mitochondrial membrane potential ($\Delta\psi$) and morphology of mitochondrial network by using TMRM and Mitotracker dyes, respectively (Fig. 1**D**). The implemented visualization strategy allows to highlight mitochondrial objects from which the area of the individual fluorescent object, the number of objects per cell and the aspect ratio of the objects can be measured.

Analysis of $TMRM^{+}$ area normalized by the $Mitotracker^{+}$ area indicated that the proportion of active mitochondria decreased by approximately 40 % in DES^{E439K}, from 80 % (79.88 ± 6.87 for Healthy control 1 and 73.52 ± 5.54 for DES^{WT}) to 45 % (58.74 ± 4.04 for DES^{HET} and 31.81 ± 1.96 for $pDES^{HET}$) as shown in Fig. 1**E** (see also supplementary Figure S3). Furthermore, we were then able to measure the number of objects per cell. DES^{E439K} hiPSC-CMs displayed a reduced number of mitochondria in comparison to WT hiPSC-CMs (Fig. 1**F**). The findings highlight that the presence of an altered desmin network is strongly correlated to mitochondrial membrane potential perturbations and a reduced number of mitochondria in cardiomyocytes.

Mitochondrial dysfunction is known to lead to a vicious cycle of cardiomyocyte dysfunction. In the same line, increased sarcomere disorganization is frequently observed in cardiomyocytes associated with genetic mutations (Eschenhagen and Carrier, 2019). hiPSC-CMs were stained using cardiac Troponin T and analyzed in each group. DES^{E439K} hiPSC-CMs showed disorganized sarcomeres, represented by diffusive sarcomere staining with no clear patterning (Fig. 1**G**, arrowhead). More specifically, 75 % of the WT hiPSC-CMs contained a highly organized sarcomere architecture (Fig. 1**G**, arrow), whereas 50–75 % of DES^{HET} and $pDES^{HET}$ hiPSC-CMs contained a partially organized sarcomere (Fig. 1**H**). With ample evidence demonstrating the involvement of mitochondria and sarcomere defect, we conclude that dysregulated desmin aggregation represents a major initial event underlying desmin-related DCM pathogenesis.

3.2. EHTs carrying DES^{E439K} recapitulate the key phenotype of DCM

Building on the morphological findings, we next evaluated the functional consequences of the mutation by assessing contractility in 3D cardiac EHT, to determine whether structural alterations translate into impaired cardiac function. Cardiac contractility is one of the most prominent aspects of heart function and is closely correlated with cardiomyopathy disease status. To further corroborate the cellular dysfunction observed in hiPSC-CMs carrying DES^{E439K} mutation and verify if it results in reduced contractile force, we used a 48-well-based 3D cardiac EHT platform, which offers more advanced and mature cardiomyocytes with functional readouts of contractility (Fig. 2**A**) (Tiburcy et al., 2017). Ring-shaped EHT was constructed from 1-month-old hiPSC-CMs and analyzed after 28 days of culture.

We first measured the spontaneous frequency of contraction (Fig. 2**B**). Most interestingly, EHTs from DES^{E439K} hiPSC-CMs displayed markedly reduced force of contraction (FOC), in comparison with WT control (Fig. 2**C**). Kinetic outputs suggested a reduction of contraction period time (Fig. 2**D**) and relaxation period time (Fig. 2**E**) but it was not significantly different from control for all DES^{E439K} clones. It appears that the rhythm variability (Fig. 2**F**) was not significantly different from

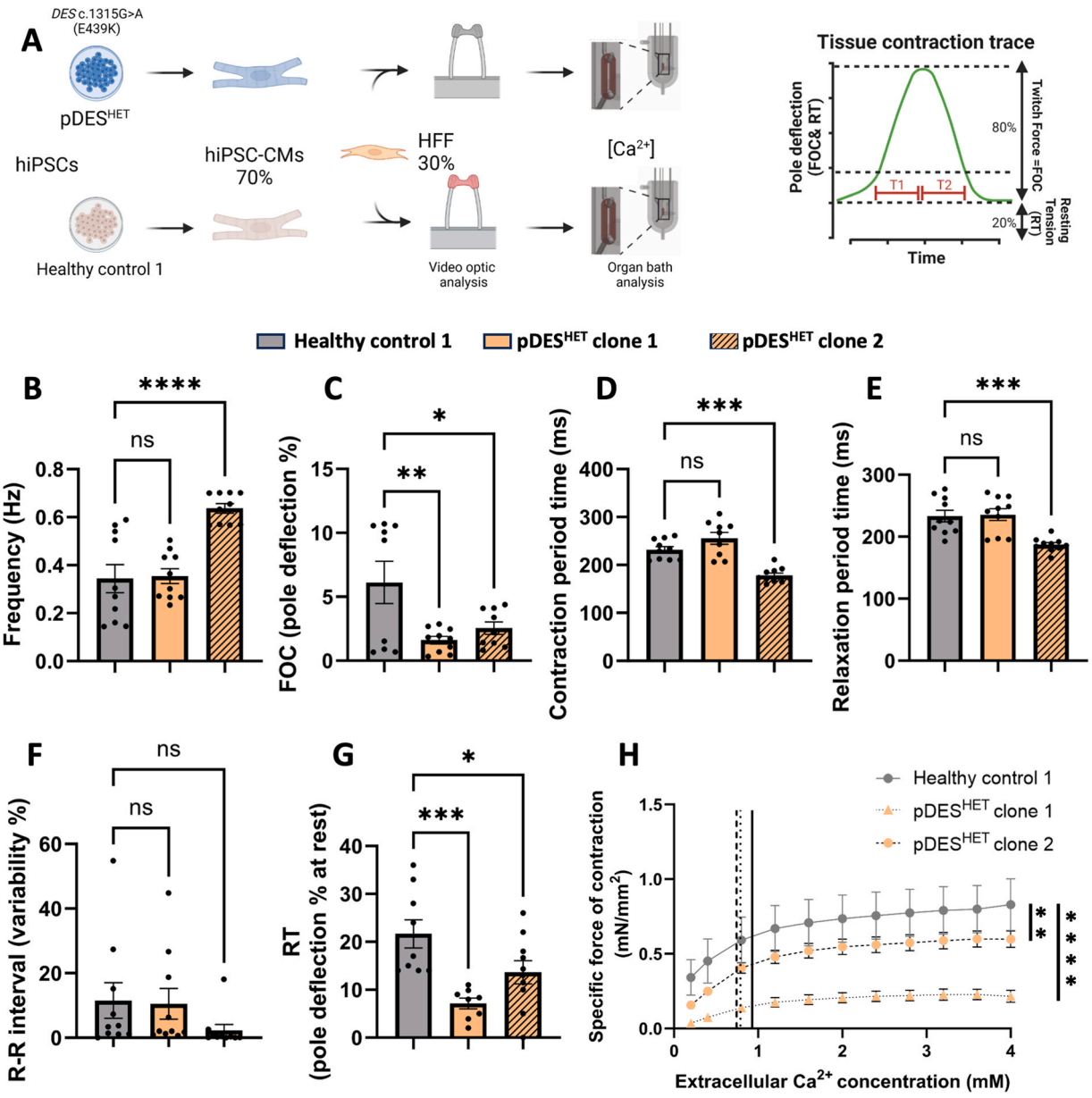

Fig. 2. Functional characterization of hiPSC-CMs carrying *DES*^{E439K} mutation using engineered heart tissues (EHTs). A. (Left) Schematic overview of the generation of EHT and characterization using video-optic and organ bath analysis. (Right) Representative contractile trace of EHT. **B.** Graph displaying frequency (Hz) for healthy EHT, pDES^{HET} clone 1 and pDES^{HET} clone 2. **C.** Graph displaying force of contraction (FOC) (as % pole bending) for healthy EHT, pDES^{HET} clone 1 and pDES^{HET} clone 2. **D.** Graph displaying contraction period time (ms) for healthy EHT, pDES^{HET} clone 1 and pDES^{HET} clone 2. **E.** Graph displaying relaxation period time (ms) healthy EHT, pDES^{HET} clone 1 and pDES^{HET} clone 2. **F.** Graph displaying R-R interval/ Rhythm (variability %) for healthy EHT, pDES^{HET} clone 1 and pDES^{HET} clone 2. **G.** Graph displaying resting time (RT) (pole deflection % at rest) for healthy EHT, pDES^{HET} clone 1 and pDES^{HET} clone 2. **H.** Specific force of contraction at increasing Ca^{2+} concentrations of healthy EHT, pDES^{HET} clone 1 and pDES^{HET} clone 2. All parameters were measured on EHT after 28 days of culture (pDES^{HET} clone 1 EHT: $n = 10$, pDES^{HET} clone 2: $n = 10$. Healthy control 1 EHT: $n = 10$). Data are presented as mean values ± SEM. Statistical significance is derived from biological replicates and determined by unpaired, two-tailed Student's *t*-test, *p* value at $^{****}p < 0.0001$, $^{***}p < 0.001$, $^{**}p < 0.01$, $^{*}p < 0.05$, and not significant (ns).

control for all *DES*^{E439K} clones suggesting that desmin is not a major contributor regarding this parameter. Resting tension (RT), a parameter referring to the initial muscle tension at rest, was significantly reduced in *DES*^{E439K} EHTs when compared with WT EHTs (Fig. 2**G**). To investigate the effect of Ca^{2+} on contractility, we measured the specific force of contraction at increasing Ca^{2+} concentrations. We found that *DES*^{E439K} EHTs had a lower specific force of contraction at all Ca^{2+} concentrations, indicating a defect in calcium handling (Fig. 2**H**). These data demonstrated that *DES*^{E439K} hiPSC-CMs produce reduced contractile force, likely due to the disruption of desmin network formation and greater fraction of cells with sarcomere deficiency and disorganization but maintain intrinsic contraction-relaxation coupling kinetics.

3.3. Transcriptomics analysis of DES^{E439K} hiPSC-CMs reveals molecular signatures of DCM

To explore the molecular mechanisms driving the observed morphological and functional abnormalities, we performed bulk RNA-sequencing of mutant and control cardiomyocytes, aiming to identify dysregulated pathways associated with the *DES*^{E439K} mutation. We performed RNA sequencing (RNA-seq) of hiPSC-CMs after culturing them in 2D monolayer and 3D EHT, as imaging-based analysis revealed

sarcomere disorganization and suggested metabolic defect, whereas functional analysis suggested that cardiomyocyte contraction is affected. Monolayer cultures were sampled at day 35 of differentiation and 3D EHT cultures at day 55 of differentiation. Cells derived from healthy individual (Healthy control 1) and *DES*^{E439K} patient (pDES^{HET}) cultured as monolayers displayed high variations and were clustered distinctly in principal component analysis (PCA). This result strongly contrasts with samples derived from isogenic hiPSC pair (DES^{WT} and DES^{HET}) that are closer in PCA (Fig. 3**A**). The replicates derived from DES^{WT} and DES^{HET} resided in proximity and separated among genotype (Fig. 3**A**). For both 3D EHT WT and *DES*^{E439K} cells derived from healthy individual (Healthy control 1) and *DES*^{E439K} patient (pDES^{HET} clone 1 and pDES^{HET} clone 2), samples were clustered distinctly in PCA and also separated among clonality and genotypes (Supplementary Figure S6A). In addition, we performed hierarchical clustering of differentially expressed genes to identify molecular signatures of the *DES*^{E439K} genotype (false discovery rate [FDR] < 0.001, Fig. 3**B** and Supplementary Figure S6B). Expression of *MYH6* and *MYH7* in both culture conditions was further validated by qPCR analysis (Supplementary Figure S6D-**E**). GO analysis demonstrated that multiple pathways involved in muscle function and differentiation, cardiac contractility, cytoskeleton, cell adhesion and junction, calcium handling and metabolism were selectively affected in *DES*^{E439K} hiPSC-CMs (Fig. 3**C-D** and Supplementary Figure S6C). Culture-type-paired analysis indicated 21 common differentially expressed genes in both 2D monolayer and 3D EHT cultures (Fig. 3**E**). STRING analysis revealed that four of these genes—*MYH11*, *COX7A1*, *ANKRD1*, and *EPHA2*—encode proteins that directly interaction with desmin (Fig. 3**F**). More specifically, MYH11 is involved in muscle contraction as part of the myosin family, while COX7A1 is a mitochondrial protein integral to the electron transport chain and oxidative phosphorylation. ANKRD1 may function as a nuclear transcription factor involved in cardiac gene regulation, and EPHA2 regulates cell adhesion and differentiation. The interaction of these genes highlights a network of structural and metabolic pathways, with a central role in intermediate filament binding, further confirming the impairment of contractility in *DES*^{E439K} models, as desmin plays a crucial role in maintaining the structural integrity of muscle fibers by linking sarcomeres to the cytoskeleton and mitochondria.

3.4. Development of an automated classifier to distinguish WT and DES^{E439K} phenotypes in hiPSC-CMs

Finally, we leveraged machine learning to integrate and generalize the phenotypic features identified across the datasets, developing a predictive model that classifies disease-related morphological patterns and may support future screening efforts. To this end, we assessed the feasibility of developing a prediction model that can be used for translational research such as screening of libraries of potential drug candidates. To this aim, we leveraged the knowledge of expert annotators in combination with measurements of desmin, cardiac Troponin T and Mitotracker patterns to develop an automated, scalable method for assessing disease stage (Fig. 4**A**). We used a three-step approach that included: 1) extraction of image features from cell morphology for each individual staining; 2) perform two-step feature selection; 3) train a classifier to distinguish WT and *DES*^{E439K} based selected features.

As an initial step toward building such prediction metrics, we created a training dataset of 48000 cells per cell line that were segmented to compute image features on desmin, Mitotracker and cardiac Troponin T stainings. Cells were segmented in order to identify a region of interest (ROI) that corresponds to a single cell based on their nuclei. Our goal was to create human interpretable features allowing us to quantify different aspects of the staining signal, including intensity, shape or texture. By calculating the average of each feature for a given cell population, the cellular profile of a hiPSC-CM can be plotted as a heatmap (Fig. 4**A**). In total, 56 features were extracted and we performed ANOVA testing to identify most statistically significant morphological features between DES and WT (Fig. 4**B**). Next, correlated features with no additional information were removed using a Pearson's correlation coefficient analysis, keeping only features with unique cellular information (Fig. 4**C**).

After performing this feature extraction and selection in WT and *DES*^{E439K} images, 23 features from desmin, 10 features from Mitotracker and 16 features from cardiac Troponin T staining were selected (Fig. 4**D**). Next, an LDA classifier was implemented to discriminate WT and *DES*^{E439K} cellular profiles using all cellular profiles generated from desmin, Mitotracker and cardiac Troponin T staining. The dataset was initially split into a training set (70 %) and a test set (30 %) before any feature selection or classifier training to prevent information leakage from the test set (Gerbin et al., 2021). From the testing set result, prediction scores of the algorithm were determined and presented in a confusion matrix (Fig. 4**E**). A machine learning evaluation (F1 score) metric showed high levels 80–100 % of accuracy of the model. As shown in the supplementary figures S7A-**C**, the values of the first LDA component strongly discriminate between WT and DES, further confirming the phenotypic difference between the two models. We then applied this classifier across the entire dataset consisting of WT and *DES*^{E439K} lines (Fig. 4**E**) and an LDA projection further demonstrated the significant differences among WT and *DES*^{E439K} phenotype (Fig. 4**F**).

4. Discussion

In this study, we assessed human iPSC-derived cardiomyocytes cultured in monolayer and 3D engineered heart tissue harboring a pathogenic *DES* mutation. Our rational was motivated by previous work of our group demonstrating the crucial role of mitochondrial abnormalities in the pathophysiology of desmin-related cardiomyopathy. The principal findings of our study are: (i) that cardiomyocytes carrying the *DES*^{E439K} variant in desmin exhibit a proteinopathy triggered by pathogenic desmin aggregation with concomitant mitochondrial and sarcomere defects and decreased contractile function; and (ii) we generated a global machine learning classifier of phenotypes based on multiple image features that is able to predict cellular pathologies. The results provided here, indicate that normal contractile function depends on the normal function and regulation of desmin.

Although our study provides valuable insights into the role of mitochondrial dysfunction and sarcomere disorganization in desmin-related cardiomyopathy, it is important to acknowledge certain limitations. Firstly, our study utilized human iPSC-CMs, which are not as mature as adult human cardiomyocytes. Our data demonstrate for the first time that under basal culture conditions, desmin was weakly expressed, which rendered a robust quantification of the phenotype difficult and demonstrated clear limitations of the cell model. However, it is known that desmin expression is low in the ventricles during the very first stages of human embryonic development (Liu et al., 2020) and increase overtime. Thus, we have used a specific culture medium (MM1) (Laco et al., 2020), known to foster maturation and in this more mature condition, desmin expression was increased. This strongly suggest that desmin seem to be required for the correct behavior of cardiomyocytes, but not for their differentiation. It also suggests that desmin could be a maturation marker of cardiomyocytes as its expression is increased with maturation. Interestingly, MM1 composition is very similar to classic RPMI+B27 medium in which T3 hormone and dexamethasone have been added, suggesting that these factors positively influence desmin expression in cardiomyocytes. Finally, in these more mature cells, we then confirmed that the desmin mutant protein is mis-localized in the cytoplasm and forms aggregates. Our study also underlines that differentiation and maturation protocols, as well as media supplements, must be carefully considered when conducting hiPSC-CM studies involving cardiomyopathies with known metabolic defects, such as mitochondrial dysfunction (*e.g.*, impaired respiration or substrate metabolism). Indeed, the level of cell differentiation and functional maturation, particularly regarding desmin expression, can significantly impact mitochondrial

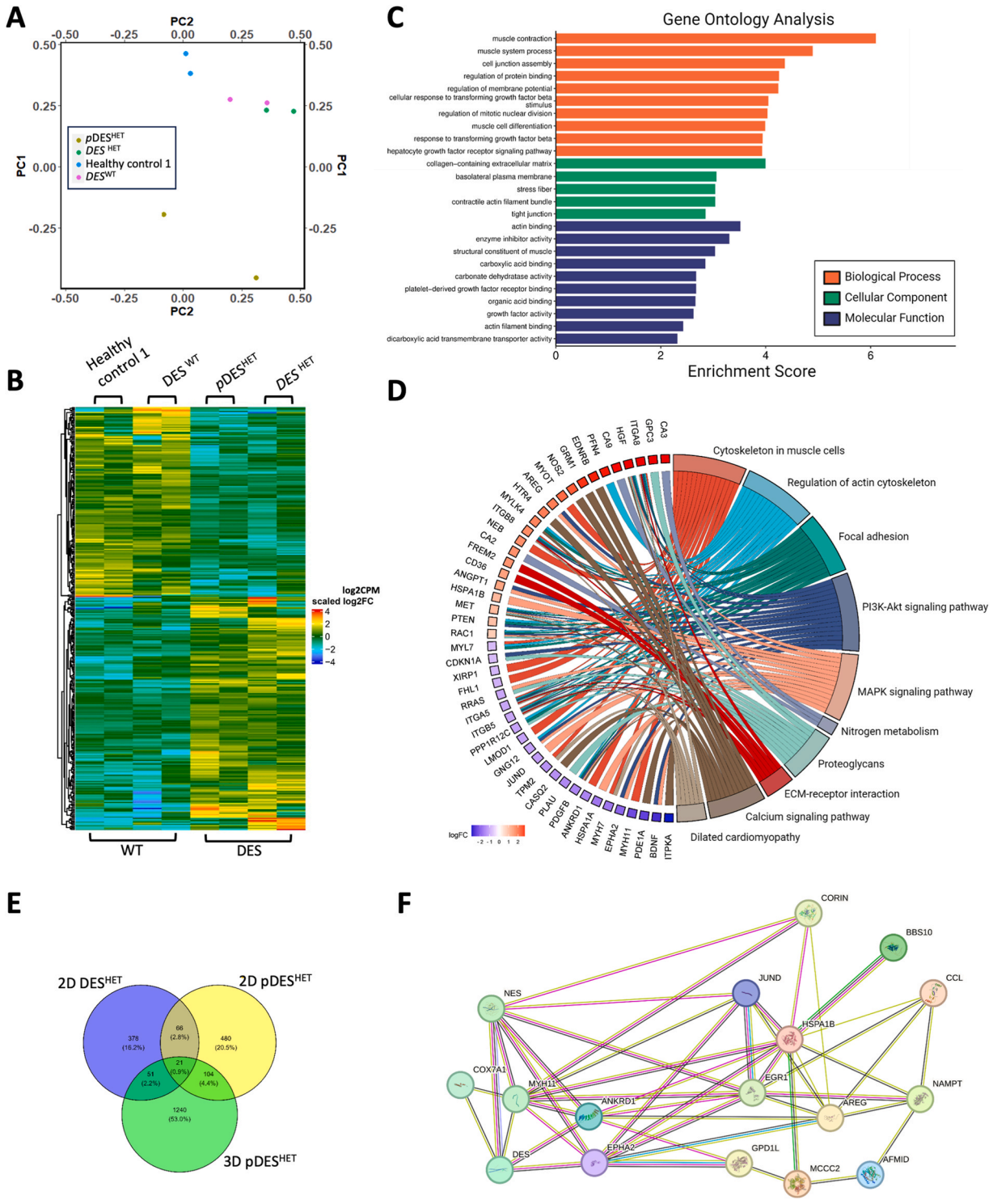

Fig. 3. Transcriptomic profiling reveals DCM signature of *DES*^{E439K} hiPSC-CMs. A. PCA analysis of 2D monolayer WT (Healthy control 1 and DES^{WT}) and *DES*^{E439K} (DES^{HET} and pDES^{HET} clone 2) hiPSC-CMs. **B.** Heatmap showing expression patterns of differentially expressed genes ($p \leq 0.05$) between 2D monolayer WT and DES hiPSC-CMs. Color scale represents scaled log2 counts per million. **C.** GO from three ontologies (biological process, cellular component and molecular function) enriched in hierarchically clustered gene subsets that changes consistently in 2D monolayer WT (Healthy control 1 and DES^{WT}) and DES (DES^{HET}) hiPSC-CMs. **D.** Circular plot of representative differentially expressed genes between 2D monolayer WT and *DES*^{E439K} hiPSC-CMs simultaneously presents a detailed view of the relations between expression changes (left semicircle perimeter) and enriched pathways (right semicircle perimeter). Color scale represents log2 fold change of gene expression originally from the RNA-seq differential gene expression analysis. **E.** Venn diagram showing unique and shared differentially expressed genes ($p \leq 0.05$) in paired analysis (2D monolayer cultures of DES^{WT} vs DES^{HET}, 2D monolayer cultures of Healthy control 1 *vs* pDES^{HET} clone 2, and 3D EHT cultures of Healthy control 1 *vs* pDES^{HET} clone 2. **F.** STRING database analysis revealing protein-protein interaction between desmin and selected dysregulated genes from E.

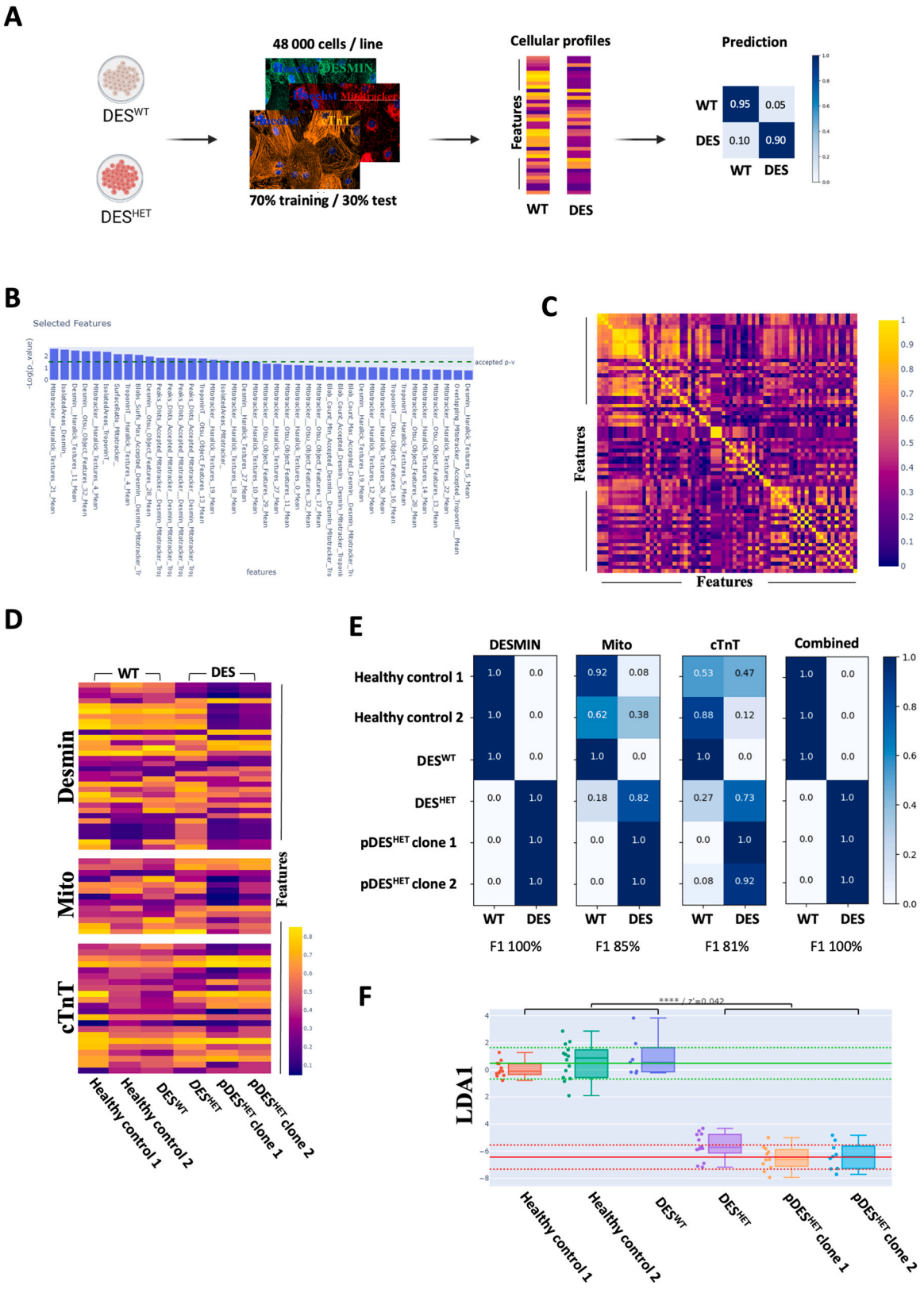

Fig. 4. A machine learning-based classification tool of disease cellular profiles. A. Schematic workflow of a two-class linear discriminant analysis (LDA) machine learning-based classification model for WT and *DES*^{E439K} hiPSC-CM cellular profiles. **B.** Selection of the relevant features based on ANOVA Test (p-value < 0.05). **C.** Exclusion of the correlated descriptors features based on Pearsons correlation. **D.** Heatmap of all selected features from each staining (desmin, Mitotracker, cardiac Troponin T) used for the cellular profiling of each hiPSC-CM. **E.** Confusion matrices of predicted label specifying the performance of the classification model. The rows correspond to the hiPSC-CM cellular profiles and the columns to the two classes (WT and *DES*^{E439K} profile) in which the model indicates the prediction score for the classification of a cellular profile in a given class. **F.** Values of the first component of trained LDA for each condition as indicated. Red area represents *DES*^{E439K} profile, whereas green area represents WT profile. A two-tailed t-test was performed. ****p-value< 0.00001.

morphology and function, as desmin mutations are linked to both structural mitochondrial abnormalities and subsequent metabolic disturbances. Secondly, using specific fluorescent probes (TMRM and Mitotracker) we estimated the status of mitochondrial function from their respective ratio of staining. Actually, these measures perfectly confirmed our previous observations on the decrease of oxygen consumption rate in mutant cardiomyocytes evaluated by Seahorse technology (Hovhannisyan et al., 2024). Moreover, we also characterized the molecular consequences of *DES* mutation through the use of RNA-seq and observed alterations of several cell function such as metabolism, cytoskeleton and muscle function. Interestingly, our study highlights a network of structural and metabolic pathways, with a central role for intermediate filament that further enrich our understanding of pathophysiological mechanism of desmin-related cardiomyopathies. Thus, the identification of key gene interactions in desmin-mutated cardiomyocytes provides crucial insights into the molecular mechanisms underlying desmin-related cardiomyopathy. STRING analysis revealed that MYH11, COX7A1, ANKRD1, and EPHA2 directly interact with desmin, all of which are associated with intermediate filament binding, a key function of desmin in maintaining the structural integrity of muscle fibers by linking sarcomeres to the cytoskeleton and mitochondria. MYH11 plays a role in muscle contraction and cytoskeletal interactions, while COX7A1, a mitochondrial protein, contributes to oxidative phosphorylation, suggesting that desmin mutations may disrupt both mechanical stability and energy production, critical for the contractile function of cardiomyocytes (Brodehl et al., 2021). In consequence, the aggregation of desmin and its interaction with key mitochondrial and contractile proteins (MYH11 and COX7A1), provides further evidence of the dual role that desmin plays in both mitochondrial function and contractile integrity (Shemer et al., 2021). Additionally, ANKRD1 and EPHA2 are involved in regulatory pathways governing cell adhesion, proliferation, and gene expression, which may indicate that desmin dysfunction triggers maladaptive signaling responses that exacerbate the pathological phenotype.

Then, a scalable, quantitative machine learning method was developed as a proof-of-concept tool to demonstrate the feasibility of such an approach to screen large number of compounds in the perspective of accelerating drug discovery for desmin-related cardiomyopathies. Thus, we successfully combined high content imaging and a machine learning prediction model that is able to predict the phenotypic state of a cardiomyocytes in culture through the quantification of multiple cellular parameters in a single assay (Hughes et al., 2021; Roukos and Misteli, 2014; Scheeder et al., 2018). It has been already shown that the association of automated fluorescence microscopy in a 384-well-plate format, image-based phenotypes and machine learning could be employed to accurately classify different states of cells (Vuidel et al., 2022). It should be noted that this strategy might be exploited for various purposes, such as disease modeling, identification of novel drug targets, or toxicity studies (Pegoraro and Misteli, 2017). Numerous studies on cardiac diseases are beginning to explore the use of high content imaging techniques to better characterize in vitro models of cardiac pathologies as well as the underlying mechanisms (Gerbin et al., 2021; Komuro et al., 2022; Sutcliffe et al., 2018). As an example, a system has been established to evaluate cardiomyocyte defects in a BAG3 model of DCM using a deep learning-based high-throughput screening assay (Yang et al., 2022). In this model they were able to demonstrate the power of combining hiPSC-CMs with phenotypic screening and deep learning as they identified HDAC6 inhibitors as cardioprotective. These technologies are very powerful and may reveal sensitives differences. It has been notably demonstrated that cardiomyocyte culturing conditions can significantly impact the ability of high content imaging to detect changes in cellular features during compound treatment (Balasubramanian et al., 2019).

In this study, we used combined features from immunostaining of different subcellular structures (desmin network, sarcomere and mitochondria). The gain in sensitivity obtained through the combination of these features is reminiscent of the cell painting strategy (Bray et al., 2016) even if our multiplexing strategy remains far from the number of features analyzed in cell painting. However, we can expect that this work could be easily translatable to other desmin mutations. Indeed, it is well known that several mutations in *DES* can trigger different pathological features such as mitochondria abnormalities, sarcomere defects and/or desmin network perturbations (Diermeier et al., 2017). Other cell structure could also be used to better assess the mechanisms and pathogenicity of the different mutations of desmin. Thus, features related to nuclei, gap junctions (through the immunostaining of connexin 43 for example) or sarcoglycan complex may strongly enrich the relevance of the classifier. Besides, it should be noticed that a two class LDA machine learning-based classification model has been chosen to develop the classification tool. LDA is relatively simple to implement and provides a linear decision boundary that is easy to understand. Moreover, while LDA makes several assumptions, it has been shown to be moderately robust to violations of these assumptions (Witten et al., 2017). Classification performance using LDA strongly depends on class labels for training, as LDA is a supervised technique. Besides, LDA is not optimized to report interactions between features or to capture complex decision boundaries. In this study, class labels are unambiguous and well-defined, indicating that LDA might perform optimally especially because our dataset is not complex nor non-linear. However, increasing the number of classes and/or features will certainly increase the complexity of datasets and may require the use of more advanced machine learning algorithms (*e.g.*, neural networks) able to capture intricate nonlinear relationships between features. Thus, even if the cell modifications triggered by the expression of mutant desmin was assessed through features related to the desmin network, the structure of sarcomere and the location and relative function of mitochondria, they were not compared to a potential toxic effect. Indeed, our classifier is not designed to attribute a cell to a toxic class (*i.e.* dead cell). However, methods to rapidly detect patterns of cardiotoxicity using high-content image analysis with deep learning and induced pluripotent stem cell-derived cardiomyocytes have been already developed (Grafton et al., 2021).

The results and technologies described here open new avenues towards a better understanding of the molecular mechanisms linked to cardiac disease manifestations of desmin mutations. They also have the potential to foster the discovery and development of new therapeutic options to address an unmet medical need.

Ethics

All the iPSC lines used in this study were generated from peripheral blood mononuclear cells (PBMC). Informed consent (written by Phenocell SAS (Grasse, France)) was obtained for the use of these PBMC and their derivatives for research in an anonymized way. This study has been approved by the CEEI/IR (ethical committee of INSERM) with the agreement number CEEI/IRB n°24–1142.

CRediT authorship contribution statement

José Américo Nabuco Leva Ferreira Freitas: Methodology, Formal analysis, Data curation. **Jochen Dobner:** Methodology, Formal analysis, Data curation. **Wiest-Daessle Nicolas:** Methodology, Formal analysis. **Konstantinos Gkatzis:** Writing – original draft, Validation, Supervision, Funding acquisition, Conceptualization. **David Hoffmann:** Methodology. **Pierre Joanne:** Writing – original draft, Validation, Supervision, Funding acquisition, Conceptualization. **Ombline Conrad:** Methodology, Formal analysis, Data curation. **Peter Sommer:** Writing – original draft, Validation, Supervision, Project administration, Funding acquisition, Conceptualization. **Jennifer Arthur Ataam:** Methodology, Formal analysis, Data curation. **Onnik Agbulut:** Writing – original draft, Validation, Supervision, Project administration, Funding acquisition, Conceptualization. **Keyhan Alvandipour:** Methodology. **Andrea Rossi:**

Methodology, Formal analysis, Data curation. **Gobert Benedicte:** Methodology. **Laurent Brino:** Supervision, Project administration. **Yeranuhi Hovhannisyan:** Methodology, Formal analysis, Data curation. **Zhenlin Li:** Writing – review & editing, Validation, Formal analysis. **Vivien Batoumeni:** Methodology, Formal analysis, Data curation. **Hakim Hocini:** Methodology, Formal analysis, Data curation.

Declaration of Competing Interest

The authors declare that they have no known competing financial interests or personal relationships that could have appeared to influence the work reported in this paper.

Acknowledgements

This work was supported by funds from Sorbonne Université, the CNRS, the INSERM, the Agence Nationale de la Recherche (ANR-21-CE19–0027-MoHeDis) and the AFM-Téléthon (contract number: 22142 & 28597). V.B. was supported by a Cifre PhD scholarship provided by Ksilink (Strasbourg) and supported by an ANRT grant (contract number: 2020/0074). JAA, KG and PS acknowledge funding by the European Union through the European Innovation Council and SMEs Executive Agency (EISMEA) in the context of the awarded grant action n. 101115536 - IMPACT - HORIZON-EIC-2022-PATHFINDERCHALLENGES-01. Ksilink was supported by the Programme d'investissements d'avenir (PIA) by the Secrétariat général pour l'investissement (SGPI) of the French government.

Appendix A. Supporting information

Supplementary data associated with this article can be found in the online version at doi:10.1016/j.ejcb.2025.151502.

Data availability

All data reported in this paper will be shared by the lead contact upon request. The RNA sequencing data generated in this study have been deposited to the sequence read archive (SRA) with the BioProject accession number PRJNA1235470. Any additional information required to reanalyze the data reported in this paper is available from the lead contact upon request.

References

Balasubramanian, B., Belak, V., Verma, I., Prysiazhniuk, Y., Sannajust, F., Trepakova, E. S., 2019. Cell culture conditions affect the ability of high content imaging assay to detect drug-induced changes in cellular parameters in human induced pluripotent stem cell-derived cardiomyocytes (hiPSC-CMs). Toxicol. Rep. 6, 305–320. https://doi.org/10.1016/j.toxrep.2019.02.004.

Bray, M.-A., Singh, S., Han, H., Davis, C.T., Borgeson, B., Hartland, C., Kost-Alimova, M., Gustafsdottir, S.M., Gibson, C.C., Carpenter, A.E., 2016. Cell Painting, a high-content image-based assay for morphological profiling using multiplexed fluorescent dyes. Nat. Protoc. 11, 1757–1774. https://doi.org/10.1038/nprot.2016.105.

Brodehl, A., Gaertner-Rommel, A., Milting, H., 2018. Molecular insights into cardiomyopathies associated with desmin (DES) mutations. Biophys. Rev. 10, 983–1006. https://doi.org/10.1007/s12551-018-0429-0.

Brodehl, A., Pour Hakimi, S.A., Stanasiuk, C., Ratnavadivel, S., Hendig, D., Gaertner, A., Gerull, B., Gummert, J., Paluszkiewicz, L., Milting, H., 2019. Restrictive cardiomyopathy is caused by a novel homozygous desmin (DES) mutation p.Y122H leading to a severe filament assembly defect. Genes 10, 918. https://doi.org/10.3390/genes10110918.

Brodehl, A., Hain, C., Flottmann, F., Ratnavadivel, S., Gaertner, A., Klauke, B., Kalinowski, J., Körperich, H., Gummert, J., Paluszkiewicz, L., Deutsch, M.-A., Milting, H., 2021. The desmin mutation DES-c.735G>C causes severe restrictive cardiomyopathy by inducing in-frame skipping of Exon-3. Biomedicines 9, 1400. https://doi.org/10.3390/biomedicines9101400.

Camman, M., Joanne, P., Agbulut, O., Hélary, C., 2022. 3D models of dilated cardiomyopathy: shaping the chemical, physical and topographical properties of biomaterials to mimic the cardiac extracellular matrix. Bioact. Mater. 7, 275–291. https://doi.org/10.1016/j.bioactmat.2021.05.040.

Capetanaki, Y., Papathanasiou, S., Diokmetzidou, A., Vatsellas, G., Tsikitis, M., 2015. Desmin related disease: a matter of cell survival failure. Curr. Opin. Cell Biol. 32, 113–120. https://doi.org/10.1016/j.ceb.2015.01.004.

Carlsson, L., Fischer, C., Sjöberg, G., Robson, R.M., Sejersen, T., Thornell, L.-E., 2002. Cytoskeletal derangements in hereditary myopathy with a desmin L345P mutation. Acta Neuropathol. 104, 493–504. https://doi.org/10.1007/s00401-002-0583-z.

Chourbagi, O., Bruston, F., Carinci, M., Xue, Z., Vicart, P., Paulin, D., Agbulut, O., 2011. Desmin mutations in the terminal consensus motif prevent synemin-desmin heteropolymer filament assembly. Exp. Cell Res. 317, 886–897. https://doi.org/10.1016/j.yexcr.2011.01.013.

Diermeier, S., Iberl, J., Vetter, K., Haug, M., Pollmann, C., Reischl, B., Buttgereit, A., Schürmann, S., Spörrer, M., Goldmann, W.H., Fabry, B., Elhamine, F., Stehle, R., Pfitzer, G., Winter, L., Clemen, C.S., Herrmann, H., Schröder, R., Friedrich, O., 2017. Early signs of architectural and biomechanical failure in isolated myofibers and immortalized myoblasts from desmin-mutant knock-in mice. Sci. Rep. 7, 1391. https://doi.org/10.1038/s41598-017-01485-x.

Ebrahim, M.A., Ali, N.M., Albash, B.Y., Al Sayegh, A.H., Ahmad, N.B., Voß, S., Klag, F., Groß, J., Holler, S., Walhorn, V., Anselmetti, D., Milting, H., Brodehl, A., 2025. Phenotypic diversity caused by the DES missense mutation p.R127P (c.380G>C) contributing to significant cardiac mortality and morbidity associated with a desmin filament assembly defect. Circ. Genom. Precis Med, e004896. https://doi.org/10.1161/CIRCGEN.124.004896.

Eschenhagen, T., Carrier, L., 2019. Cardiomyopathy phenotypes in human-induced pluripotent stem cell-derived cardiomyocytes-a systematic review. Pflug. Arch. 471, 755–768. https://doi.org/10.1007/s00424-018-2214-0.

Feyen, Dries A.M., McKeithan, W.L., Bruyneel, A.A.N., Spiering, S., Hörmann, L., Ulmer, B., Zhang, H., Briganti, F., Schweizer, M., Hegyi, B., Liao, Z., Pölönen, R.-P., Ginsburg, K.S., Lam, C.K., Serrano, R., Wahlquist, C., Kreymerman, A., Vu, M., Amatya, P.L., Behrens, C.S., Ranjbarvaziri, S., Maas, R.G.C., Greenhaw, M., Bernstein, D., Wu, J.C., Bers, D.M., Eschenhagen, T., Metallo, C.M., Mercola, M., 2020. Metabolic maturation media improve physiological function of human ipsc-derived cardiomyocytes. Cell Rep. 32, 107925. https://doi.org/10.1016/j.celrep.2020.107925.

Gerbin, K.A., Grancharova, T., Donovan-Maiye, R.M., Hendershott, M.C., Anderson, H. G., Brown, J.M., Chen, J., Dinh, S.Q., Gehring, J.L., Johnson, G.R., Lee, H., Nath, A., Nelson, A.M., Sluzewski, M.F., Viana, M.P., Yan, C., Zaunbrecher, R.J., Cordes Metzler, K.R., Gaudreault, N., Knijnenburg, T.A., Rafelski, S.M., Theriot, J.A., Gunawardane, R.N., 2021. Cell states beyond transcriptomics: Integrating structural organization and gene expression in hiPSC-derived cardiomyocytes. Cell Syst. 12, 670–687.e10. https://doi.org/10.1016/j.cels.2021.05.001.

Goldfarb, L.G., Park, K.-Y., Cervenáková, L., Gorokhova, S., Lee, H.-S., Vasconcelos, O., Nagle, J.W., Semino-Mora, C., Sivakumar, K., Dalakas, M.C., 1998. Missense mutations in desmin associated with familial cardiac and skeletal myopathy. Nat. Genet 19, 402–403. https://doi.org/10.1038/1300.

Grafton, F., Ho, J., Ranjbarvaziri, S., Farshidfar, F., Budan, A., Steltzer, S., Maddah, M., Loewke, K.E., Green, K., Patel, S., Hoey, T., Mandegar, M.A., 2021. Deep learning detects cardiotoxicity in a high-content screen with induced pluripotent stem cell-derived cardiomyocytes. eLife 10, e68714. https://doi.org/10.7554/eLife.68714.

Hnia, K., Ramspacher, C., Vermot, J., Laporte, J., 2015. Desmin in muscle and associated diseases: beyond the structural function. Cell Tissue Res 360, 591–608. https://doi.org/10.1007/s00441-014-2016-4.

Hovhannisyan, Y., Li, Z., Callon, D., Suspène, R., Batoumeni, V., Canette, A., Blanc, J., Hocini, H., Lefebvre, C., El-Jahrani, N., Kitsara, M., L'honoré, A., Kordeli, E., Fornes, P., Concordet, J.-P., Tachdjian, G., Rodriguez, A.-M., Vartanian, J.-P., Béhin, A., Wahbi, K., Joanne, P., Agbulut, O., 2024. Critical contribution of mitochondria in the development of cardiomyopathy linked to desmin mutation. Stem Cell Res Ther. 15, 1–23. https://doi.org/10.1186/s13287-023-03619-7.

Hughes, R.E., Elliott, R.J.R., Dawson, J.C., Carragher, N.O., 2021. High-content phenotypic and pathway profiling to advance drug discovery in diseases of unmet need. Cell Chem. Biol. 28, 338–355. https://doi.org/10.1016/j.chembiol.2021.02.015.

Joanne, P., Chourbagi, O., Hourdé, C., Ferry, A., Butler-Browne, G., Vicart, P., Dumonceaux, J., Agbulut, O., 2013. Viral-mediated expression of desmin mutants to create mouse models of myofibrillar myopathy. Skelet. Muscle 3, 4. https://doi.org/10.1186/2044-5040-3-4.

Komuro, J., Tokuoka, Y., Seki, T., Kusumoto, D., Hashimoto, H., Katsuki, T., Nakamura, T., Akiba, Y., Kuoka, T., Kimura, M., Yamada, T., Fukuda, K., Funahashi, A., Yuasa, S., 2022. Development of non-bias phenotypic drug screening for cardiomyocyte hypertrophy by image segmentation using deep learning. Biochem. Biophys. Res. Commun. 632, 181–188. https://doi.org/10.1016/j.bbrc.2022.09.108.

Laco, F., Lam, A.T.-L., Woo, T.-L., Tong, G., Ho, V., Soong, P.-L., Grishina, E., Lin, K.-H., Reuveny, S., Oh, S.K.-W., 2020. Selection of human induced pluripotent stem cells lines optimization of cardiomyocytes differentiation in an integrated suspension microcarrier bioreactor. Stem Cell Res Ther. 11, 118. https://doi.org/10.1186/s13287-020-01618-6.

Lian, X., Hsiao, C., Wilson, G., Zhu, K., Hazeltine, L.B., Azarin, S.M., Raval, K.K., Zhang, J., Kamp, T.J., Palecek, S.P., 2012. Robust cardiomyocyte differentiation from human pluripotent stem cells via temporal modulation of canonical Wnt signaling. Proc. Natl. Acad. Sci. U. S. A. 109, E1848–E1857. https://doi.org/10.1073/pnas.1200250109.

Liu, H.-X., Jing, Y.-X., Wang, J.-J., Yang, Y.-P., Wang, Y.-X., Li, H.-R., Song, L., Li, A.-H., Cui, H.-L., Jing, Y., 2020. Expression patterns of intermediate filament proteins desmin and lamin A in the developing conduction system of early human embryonic hearts. J. Anat. 236, 540–548. https://doi.org/10.1111/joa.13108.

Pegoraro, G., Misteli, T., 2017. High-throughput imaging for the discovery of cellular mechanisms of disease. Trends Genet. 33, 604–615. https://doi.org/10.1016/j.tig.2017.06.005.

Roukos, V., Misteli, T., 2014. Deep imaging: the next frontier in microscopy. Histochem Cell Biol. 142, 125–131. https://doi.org/10.1007/s00418-014-1239-5.

Scheeder, C., Heigwer, F., Boutros, M., 2018. Machine learning and image-based profiling in drug discovery. current opinion in systems biology. Pharmacol. Drug Discov. 10, 43–52. https://doi.org/10.1016/j.coisb.2018.05.004.

Schultheiss, H.-P., Fairweather, D., Caforio, A.L.P., Escher, F., Hershberger, R.E., Lipshultz, S.E., Liu, P.P., Matsumori, A., Mazzanti, A., McMurray, J., Priori, S.G., 2019. Dilated cardiomyopathy. Nat. Rev. Dis. Prim. 5, 32. https://doi.org/10.1038/s41572-019-0084-1.

Shemer, Y., Mekies, L.N., Ben Jehuda, R., Baskin, P., Shulman, R., Eisen, B., Regev, D., Arbustini, E., Gerull, B., Gherghiceanu, M., Gottlieb, E., Arad, M., Binah, O., 2021. Investigating LMNA-related dilated cardiomyopathy using human induced pluripotent stem cell-derived cardiomyocytes. Int J. Mol. Sci. 22, 7874. https://doi.org/10.3390/ijms22157874.

Smolina, N., Khudiakov, A., Knyazeva, A., Zlotina, A., Sukhareva, K., Kondratov, K., Gogvadze, V., Zhivotovsky, B., Sejersen, T., Kostareva, A., 2020. Desmin mutations result in mitochondrial dysfunction regardless of their aggregation properties. Biochim Biophys. Acta Mol. Basis Dis. 1866, 165745. https://doi.org/10.1016/j.bbadis.2020.165745.

Sutcliffe, M.D., Tan, P.M., Fernandez-Perez, A., Nam, Y.-J., Munshi, N.V., Saucerman, J. J., 2018. High content analysis identifies unique morphological features of reprogrammed cardiomyocytes. Sci. Rep. 8, 1258. https://doi.org/10.1038/s41598-018-19539-z.

Tiburcy, M., Hudson, J.E., Balfanz, P., Schlick, S., Meyer, T., Chang Liao, M.-L., Levent, E., Raad, F., Zeidler, S., Wingender, E., Riegler, J., Wang, M., Gold, J.D., Kehat, I., Wettwer, E., Ravens, U., Dierickx, P., Van Laake, L.W., Goumans, M.J., Khadjeh, S., Toischer, K., Hasenfuss, G., Couture, L.A., Unger, A., Linke, W.A., Araki, T., Neel, B., Keller, G., Gepstein, L., Wu, J.C., Zimmermann, W.-H., 2017. Defined engineered human myocardium with advanced maturation for applications in heart failure modeling and repair. Circulation 135, 1832–1847. https://doi.org/10.1161/CIRCULATIONAHA.116.024145.

Tsikitis, M., Galata, Z., Mavroidis, M., Psarras, S., Capetanaki, Y., 2018. Intermediate filaments in cardiomyopathy. Biophys. Rev. 10, 1007–1031. https://doi.org/10.1007/s12551-018-0443-2.

Vuidel, A., Cousin, L., Weykopf, B., Haupt, S., Hanifehlou, Z., Wiest-Daesslé, N., Segschneider, M., Lee, J., Kwon, Y.-J., Peitz, M., Ogier, A., Brino, L., Brüstle, O., Sommer, P., Wilbertz, J.H., 2022. High-content phenotyping of Parkinson's disease patient stem cell-derived midbrain dopaminergic neurons using machine learning classification. Stem Cell Rep. 17, 2349–2364. https://doi.org/10.1016/j.stemcr.2022.09.001.

Wang, X., Osinska, H., Dorn, G.W., Nieman, M., Lorenz, J.N., Gerdes, A.M., Witt, S., Kimball, T., Gulick, J., Robbins, J., 2001. Mouse model of desmin-related cardiomyopathy. Circulation 103, 2402–2407. https://doi.org/10.1161/01.CIR.103.19.2402.

Witten, I.H., Frank, E., Hall, M.A., Pal, C.J., 2017. Chapter 8 - Data transformations, in: Witten, I.H., Frank, E., Hall, M.A., Pal, C.J. (Eds.), Data Mining (Fourth Edition). Morgan Kaufmann, pp. 285–334. https://doi.org/10.1016/B978-0-12-804291-5.00008-8.

Yang, J., Grafton, F., Ranjbarvaziri, S., Budan, A., Farshidfar, F., Cho, M., Xu, E., Ho, J., Maddah, M., Loewke, K.E., Medina, J., Sperandio, D., Patel, S., Hoey, T., Mandegar, M.A., 2022. Phenotypic screening with deep learning identifies HDAC6 inhibitors as cardioprotective in a BAG3 mouse model of dilated cardiomyopathy. eabl5654 Sci. Transl. Med 14. https://doi.org/10.1126/scitranslmed.abl5654.